

## Geometric integration of guiding-center orbits in piecewise linear toroidal fields

M. Eder<sup>1</sup>, C.G. Albert<sup>2</sup>, L.M.P. Bauer<sup>1</sup>, S.V. Kasilov<sup>1,3</sup>, W. Kernbichler<sup>1</sup>

<sup>1</sup> *Fusion@ÖAW, Institut für Theoretische Physik - Computational Physics,  
Technische Universität Graz, Petersgasse 16, 8010 Graz,  
Austria*

<sup>2</sup> *Max-Planck-Institut für Plasmaphysik, Boltzmannstr. 2, 85748 Garching,  
Germany*

<sup>3</sup> *Institute of Plasma Physics, National Science Center  
“Kharkov Institute of Physics and Technology”, 61108, Kharkov,  
Ukraine*

A geometric integration method for guiding-center orbits of charged particles in toroidal fusion devices with three-dimensional field geometry is described. Here, high order interpolation of electromagnetic fields in space is replaced by a special linear interpolation, leading to locally linear Hamiltonian equations of motion with piecewise constant coefficients. This approach reduces computational effort and noise sensitivity while the conservation of total energy, magnetic moment and phase space volume is retained. When applied to collisionless guiding-center orbits in an axisymmetric tokamak and a realistic three-dimensional stellarator configuration, the method demonstrates correct long-term orbit dynamics. Within Monte Carlo evaluation of transport coefficients, the computational efficiency of geometric integration is an order of magnitude higher than with a standard adaptive Runge-Kutta integrator.

*Key words:* plasma physics; kinetic modeling; numerical integration; Hamiltonian systems; guiding-center dynamics; magnetic confinement;

## I. INTRODUCTION

Global kinetic computations of quasi-steady plasma parameters in 3D toroidal fusion devices utilize the evaluation of the distribution function and/or its moments by direct modeling of particle orbits. This includes Monte Carlo transport simulations in given external fields<sup>1–9</sup> as well as self-consistent turbulence models with particle codes.<sup>10–13</sup> Kinetic modeling of 3D plasma equilibria<sup>14</sup> or edge plasmas<sup>15</sup> puts specific requirements on solving the guiding-center equations.<sup>16–18</sup> Namely, particle orbit integration should be computationally efficient, tolerant to statistical noise in the electromagnetic field and efficient in scoring statistical data from the orbits. Geometric integrators<sup>19,20</sup> address these targets by relaxing the requirement to the accuracy of guiding-center orbits while preserving physically correct long time orbit dynamics. In this context the word geometric refers to the preservation of the geometric structure of phase-space being a symplectic manifold. The most well-known class of geometric integrators are symplectic integrators that rely on canonical coordinates in phase-space. Symplectic integrators are not directly applicable to guiding-center dynamics that are formulated in non-canonical coordinates. One way to circumvent this problem is the use of a (usually implicit) transformation to canonical coordinates.<sup>21–23</sup> Up to now such approaches rely either on magnetic flux coordinates or require a more expensive transformation of phase-space coordinates in the general case. The other known alternative are variational integrators.<sup>24,25</sup> Such integrators do not assume canonical coordinates and include symplectic integrators as a special case. Stability problems of variational integrators arise for guiding-center orbit computations due to the degeneracy of their phase-space Lagrangian. This issue has only recently been resolved.<sup>26–28</sup> The resulting integrators are fully implicit and/or require an augmented set of dynamical variables, and their competitiveness for practical applications is still a topic open to investigation.

The method presented here is geometric in both, a structure-preserving and a more literal sense, as it considers intersections of orbits with a spatial mesh. It has been introduced in Ref. 29 as a generalization of the 2D geometric integrator of Ref. 30 for general 3D toroidal fields. This approach has two features useful for application in global equilibrium and transport simulations: straightforward computation of spatial distributions of macroscopic parameters and robustness in the presence of noise in field data. Moreover, the new method preserves total energy, magnetic moment and phase space volume.

The integration procedure is based on a special 3D discretization of space resulting in piecewise linear guiding-center equations while retaining the symplectic property of the original set. Within this discretization, vectors and scalars characterizing the electromagnetic field are represented by continuous piecewise linear functions which reduces the cost of spatial interpolation as compared to high-order interpolation with continuous derivatives (e.g. with help of 3D-splines) required for usual integration. In return, the integration procedure requires accurate tracing of intersections of the orbit with spatial cell boundaries where the coefficients of the linear guiding-center equation set are discontinuous. However, tracing of the boundaries is also required in Monte Carlo procedures for the computation of the spatial distribution of various velocity space moments of the distribution function which are computed as path integrals over the test particle dwell time within spatial cells.

In the original implementation of Ref. 29, the linear guiding-center equation set was solved numerically by using a usual Runge-Kutta (RK) integrator. In this case, tracing of orbit intersections with spatial cell boundaries requires a few Newton iterations for the computation of the dwell time within the cell. Since the integration error of this set scales with the third power of the Larmor radius, accurate results can still be obtained by a single RK integration step over the dwell time. For the same reason, sufficient accuracy can be achieved also by using the polynomial expansion of the solution over the dwell time which allows to compute this time and integrals of velocity powers analytically.

In case of magnetic fields with spatial symmetry (e.g., tokamaks with toroidal symmetry) the geometric integration accurately preserves the respective (toroidal) canonical momentum. Thus, the property of such systems to ideally confine the orbits is retained. In absence of spatial symmetry, the parallel adiabatic invariant, which is an approximate conserved quantity in stellarators, is well preserved, since the geometric integration does not lead to a significant error accumulation.

It should be noted that the piecewise linear approximation of the guiding-center equations represents field lines as polygonal chains in coordinate space. Such a representation may introduce artificial chaos in case of 3D fields when using non-aligned coordinate systems. In our earlier publication<sup>29</sup>, some field line diffusion has been observed in a perturbed tokamak field which seemed to be in agreement with the quasilinear estimate assuming a continuous safety factor profile of the unperturbed field (which is, actually, not the case), and, therefore, this diffusion has been attributed to the linearization. However, further detailed studies

and resulting improvements of the algorithm revealed that the level of artificial diffusion observed earlier is not connected with the intrinsic deficiency of the method. In the improved algorithm this diffusion is actually much smaller so that it provides a negligible correction to the existing neoclassical transport even for rather strongly perturbed non-aligned 3D fields and a coarse mesh.

The above mentioned characteristics of the method allow, in particular, its effective application to the computation of neoclassical transport coefficients using the Monte Carlo method. For demonstration, the mono-energetic neoclassical diffusion coefficient is evaluated here for a quasi-isodynamic reactor-scale stellarator field<sup>31</sup>. The results and performance of the new method are compared to usual (RK) orbit integration methods.

The remainder of this article is organized as follows. In section II the spatial discretization procedure is introduced and the numerical solution of the resulting piecewise linear guiding-center equations is described. In section III single particle orbits obtained with the geometric integration method and respective invariants of motion for axisymmetric and non-axisymmetric geometries are analyzed in detail. **Furthermore, the introduced artificial chaos is studied.** The method's application to the evaluation of transport coefficients is presented in section IV, where the computational orbit-integration performance is benchmarked as well. Finally, the conclusion from the present study and further outlook is given in section V.

## II. DERIVATION OF THE ORBIT INTEGRATION METHOD AND NUMERICAL SOLUTION

### A. Locally linear Hamiltonian guiding-center equations

As a starting point, the equations of guiding-center motion<sup>17</sup> in general curvilinear coordinates  $x^i$  are

$$\dot{x}^i = \frac{v_{\parallel} \varepsilon^{ijk}}{\sqrt{g} B_{\parallel}^*} \frac{\partial A_k^*}{\partial x^j}, \quad A_k^* = A_k + \frac{v_{\parallel}}{\omega_c} B_k. \quad (1)$$

Here,  $A_k$ ,  $B_k$ ,  $\omega_c$ ,  $\Phi$  and  $\sqrt{g}$  are the covariant components of the vector potential and the magnetic field, cyclotron frequency, electrostatic potential and the metric determinant, respectively, and  $\sqrt{g} B_{\parallel}^* = \varepsilon^{ijk} (B_i/B) \partial A_k^* / \partial x^j$ . Charge  $e_{\alpha}$  and mass  $m_{\alpha}$  of the considered

species  $\alpha$  enter  $\omega_c = e_\alpha B / (m_\alpha c)$  together with the magnetic field modulus  $B = \sqrt{B_k B^k}$  and the speed of light  $c$ . The equations of motion are considered with the invariants  $w = m_\alpha v^2/2 + e_\alpha \Phi$  and  $J_\perp = m_\alpha v_\perp^2/(2\omega_c)$  being total energy and perpendicular adiabatic invariant, respectively, and used as independent phase space variables. The parallel velocity  $v_\parallel$  in (1) is not an independent variable but a known function of coordinates,

$$v_\parallel^2 = 2U, \quad U = U(\mathbf{x}) = \frac{1}{m} (w - J_\perp \omega_c(\mathbf{x}) - e_\alpha \Phi(\mathbf{x})). \quad (2)$$

Treating  $v_\parallel$  as an independent variable now, i.e. replacing the first expression of (2) by the differential equation

$$\dot{v}_\parallel = \frac{1}{v_\parallel} \dot{x}^i \frac{\partial U}{\partial x^i}, \quad (3)$$

the set (1) turns into

$$\begin{aligned} B_\parallel^* \sqrt{g} \dot{x}^i &= \frac{dx^i}{d\tau} = \varepsilon^{ijk} \left( v_\parallel \frac{\partial A_k}{\partial x^j} + 2U \frac{\partial}{\partial x^j} \frac{B_k}{\omega_c} + \frac{B_k}{\omega_c} \frac{\partial U}{\partial x^j} \right), \\ B_\parallel^* \sqrt{g} \dot{v}_\parallel &= \frac{dv_\parallel}{d\tau} = \varepsilon^{ijk} \frac{\partial U}{\partial x^i} \left( \frac{\partial A_k}{\partial x^j} + v_\parallel \frac{\partial}{\partial x^j} \frac{B_k}{\omega_c} \right). \end{aligned} \quad (4)$$

Note that the invariants of motion remain in (4) as parameters entering the function of coordinates  $U$  defined by the second expression of (2). In (4) the time variable is replaced by an orbit parameter  $\tau$  related to time by  $dt = B_\parallel^* \sqrt{g} d\tau$ , and the time evolution is obtained implicitly from the integral  $t(\tau)$ .

The special form (4) allows to reduce computational effort and noise sensitivity by independently approximating the field quantities  $A_k$ ,  $B_k/\omega_c$ ,  $\omega_c$  and  $\Phi$  by continuous piecewise linear functions. Thus, curvilinear coordinate space is split into tetrahedral cells with exact field values on the cell's vertices. Fig. 1 depicts such a curvilinear field-aligned grid for the plasma core of a tokamak, where splitting along the symmetry direction is achieved with stackable hexahedra, each consisting of six tetrahedral cells. As a result, in each cell, the equations of motion (4) turn into a set of four linear ODEs with constant coefficients

$$\frac{dz^i}{d\tau} = a_l^i z^l + b^i, \quad (5)$$

in phase-space variables  $z^i = x^i$  for  $i = 1, 2, 3$  and  $z^4 = v_{\parallel}$ . The matrix elements are

$$\begin{aligned} a_l^i &= \varepsilon^{ijk} \left( 2 \frac{\partial U}{\partial x^l} \frac{\partial}{\partial x^j} \frac{B_k}{\omega_c} + \frac{\partial U}{\partial x^j} \frac{\partial}{\partial x^l} \frac{B_k}{\omega_c} \right) \quad \text{for} \quad 1 \leq i, l \leq 3, \\ a_4^i &= \varepsilon^{ijk} \frac{\partial A_k}{\partial x^j} \quad \text{for} \quad 1 \leq i \leq 3, \\ a_l^4 &= 0 \quad \text{for} \quad 1 \leq l \leq 3, \\ a_4^4 &= \varepsilon^{ijk} \frac{\partial U}{\partial x^i} \frac{\partial}{\partial x^j} \frac{B_k}{\omega_c}, \end{aligned} \quad (6)$$

and components of vector  $b^i$  are

$$\begin{aligned} b^i &= \varepsilon^{ijk} \left( 2U_0 \frac{\partial}{\partial x^j} \frac{B_k}{\omega_c} + \left( \frac{B_k}{\omega_c} \right)_0 \frac{\partial U}{\partial x^j} \right) \quad \text{for} \quad 1 \leq i \leq 3, \\ b^4 &= \varepsilon^{ijk} \frac{\partial U}{\partial x^i} \frac{\partial A_k}{\partial x^j}, \end{aligned} \quad (7)$$

where quantities with zero mean the value at the origin of the coordinates,

$$U = U_0 + x^i \frac{\partial U}{\partial x^i}, \quad \frac{B_k}{\omega_c} = \left( \frac{B_k}{\omega_c} \right)_0 + x^i \frac{\partial}{\partial x^i} \frac{B_k}{\omega_c}. \quad (8)$$

Since the piecewise constant coefficients of set (5) are discontinuous at the cell boundaries, orbit intersections with tetrahedra faces must be computed exactly when integrating particle trajectories.

In fact, a linear approximation of field quantities which locally breaks the physical connection between them does not destroy the Hamiltonian nature of the original set (1). Indeed, despite the approximation made, equation set (4) can still be cast to the non-canonical Hamiltonian form

$$\frac{dz^i}{d\tau} = \Lambda^{ij} \frac{\partial H}{\partial z^j}, \quad \Lambda^{ij}(\mathbf{z}) = \{z^i, z^j\}_{\tau}, \quad (9)$$

where the Hamiltonian function is  $H(\mathbf{z}) = v_{\parallel}^2/2 - U(\mathbf{x})$  and  $\Lambda^{ij}(\mathbf{z})$  is an antisymmetric Poisson matrix. The latter is linked to Poisson brackets that are slightly re-defined from those in Ref. 32 due to a different orbit parameter,

$$\{f, g\}_{\tau} = b_*^i \left( \frac{\partial f}{\partial x^i} \frac{\partial g}{\partial v_{\parallel}} - \frac{\partial g}{\partial x^i} \frac{\partial f}{\partial v_{\parallel}} \right) + \varepsilon^{ijk} \frac{\partial g}{\partial x^i} \frac{\partial f}{\partial x^j} \frac{B_k}{\omega_c}, \quad b_*^i = \varepsilon^{ijk} \left( \frac{\partial A_k}{\partial x^j} + v_{\parallel} \frac{\partial}{\partial x^j} \frac{B_k}{\omega_c} \right). \quad (10)$$

In the derivation above, one occurrence of  $v_{\parallel}^2$  has been replaced by  $2U(\mathbf{x})$  to obtain equation set (4). As long as this equality in the first of (2) is kept exact by a numerical scheme, a geometric Poisson integrator follows, being a generalization of symplectic integrators in non-canonical coordinates. Similar to symplectic integrators, Poisson integrators preserve the symplectic structure and invariants of motion within fixed bounds.<sup>19</sup>

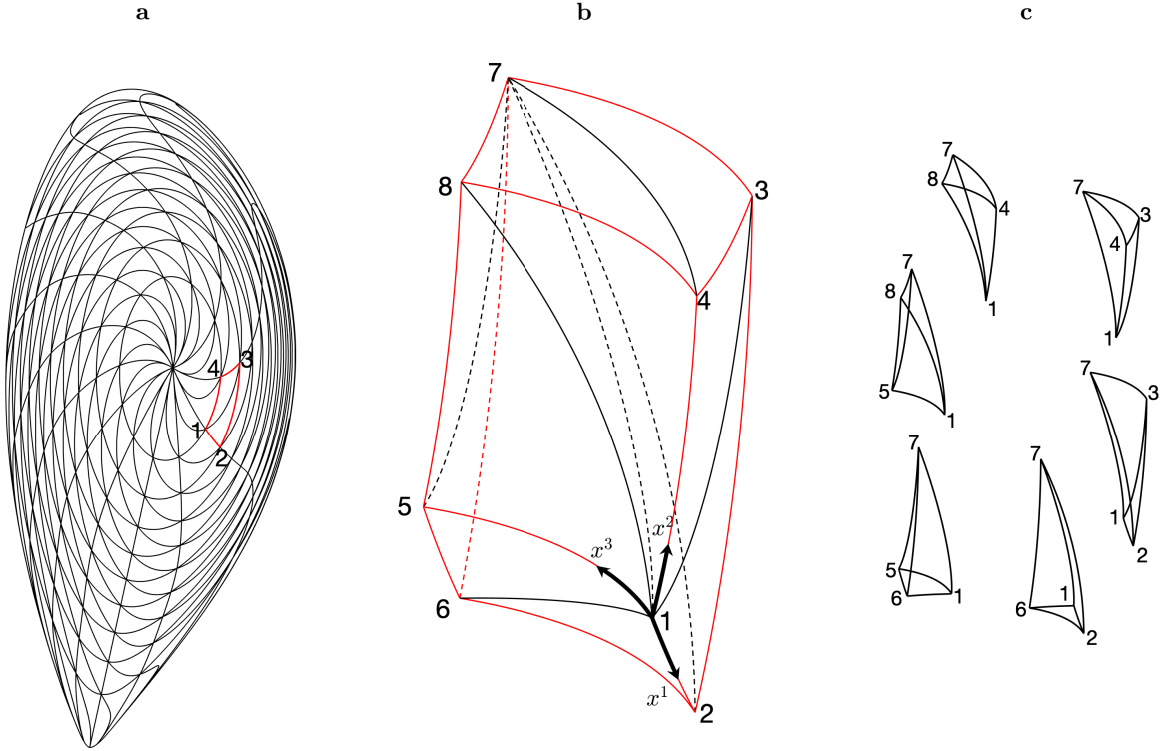


FIG. 1: Real space illustration of field-aligned grid for the plasma core of a toroidal fusion device. Magnetic field lines are traced in general curvilinear coordinates  $(x^1, x^2, x^3)$  on  $N_s$  flux surfaces. At equidistant spacing in toroidal and poloidal direction a 3D grid consisting of  $N_s \times N_\theta \times N_\varphi$  hexahedra is created. (a) 2D poloidal projection of 3D grid with a marked hexahedron cell. (b) Magnification of marked hexahedron in (a) with indication how each hexahedron is split into six tetrahedral cells. Resulting tetrahedra are oriented in symmetry direction  $x^3$  such that linear interpolation of electromagnetic field enables exact field representation on the cell's vertices. (c) Six individual tetrahedral cells compose stackable hexahedron such that adjacent tetrahedra faces are congruent.

## B. Numerical solution

An approximate formal solution of set (5) in a single cell is given as a polynomial series of the orbit parameter,

$$\mathbf{z}(\tau) = \mathbf{z}_0 + \sum_{k=1}^K \frac{\tau^k}{k!} (\hat{\mathbf{a}}^{k-1} \cdot \mathbf{b} + \hat{\mathbf{a}}^k \cdot \mathbf{z}_0), \quad (11)$$

where  $\hat{\mathbf{a}}$  and  $\mathbf{b}$  stand for matrix  $a_l^i$  and vector  $b^i$ , respectively,  $\mathbf{z}(0) = \mathbf{z}_0$  is a starting point, and the exact solution is obtained in the limit  $K \rightarrow \infty$ . Since intersections with cell

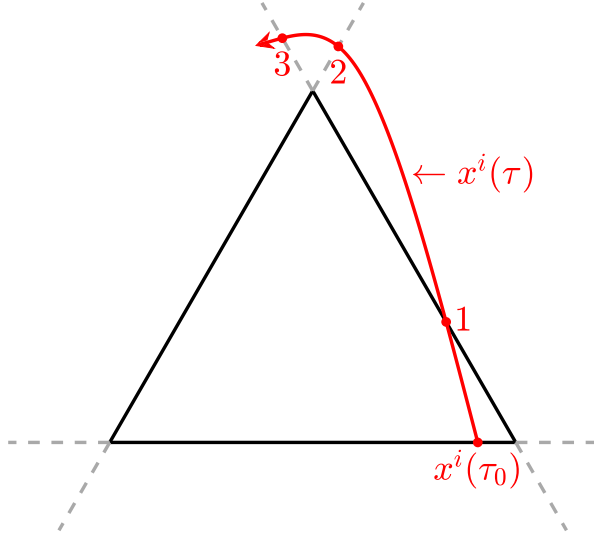


FIG. 2: Illustration of intersections of the orbit  $x^i(\tau)$  with planes confining the cell. For simplification, the three-dimensional tetrahedral cell is depicted as a two-dimensional triangle. The particle enters the cell at  $x^i(\tau_0)$  and leaves the cell at ①. Other intersections at the points ② and ③ are not realized. The correct orbit-tetrahedron intersection ① is reached in the smallest positive time among all intersections.

boundaries (tetrahedra faces) must be computed exactly, the particle is pushed from cell boundary to cell boundary, if no intermediate position inside a cell, e.g. after a pre-defined time step, is required deliberately. An orbit intersection with a tetrahedron is found on exit as an intersection with one of four planes

$$F^\alpha(\mathbf{z}) \equiv n_i^{(\alpha)} (x^i - x_{(\alpha)}^i) = 0, \quad \alpha = 1, \dots, 4 \quad (12)$$

reached in the smallest positive time after entry (“dwell time”), see Fig. 2. Here,  $n_i^{(\alpha)}$  and  $x_{(\alpha)}^i$  are the (constant) normal to the plane containing tetrahedron face  $\alpha$  and coordinates of some vertex on that face, respectively. With substitution of the orbit,  $\mathbf{z} = \mathbf{z}(\tau)$ , Eqs. (12) are nonlinear equations with respect to the orbit parameter,  $F^\alpha(\mathbf{z}(\tau)) = 0$ , which should be solved numerically. They become algebraic and can be solved analytically if an approximate solution (11) is used with  $K \leq 4$ .

Both cases have been implemented in a Fortran program with the name **Geometric ORbit Integration with Local Linearisation Approach (Gorilla)**.

In its first variant (*Gorilla RK4*), the orbit intersections with tetrahedra faces are computed numerically by solving equation set (5) in each cell with a single step of the Runge-Kutta 4 method embedded into an iterative scheme using Newton’s method to obtain the integration time  $\Delta\tau$  required to reach the cell boundary (dwell time  $\tau_d = \Delta\tau$ ). Predominantly, this iterative scheme converges after roughly two Newton iterations, due to an analytic estimation for the necessary initial step length using an approximate parabolic solution of ODE set (5) taken in zeroth order in Larmor radius,  $a_l^i = 0$  for  $1 \leq i, j \leq 3$  and  $a_4^4 v_{\parallel}(\tau) = a_4^4 v_{\parallel,0}$ .

Nevertheless, in case of numerically challenging orbits (tangential to a tetrahedron face or almost intersecting with a tetrahedron's edges or vertices), several special cases appear where the iterative scheme doesn't converge, and those cases must be treated separately in a computationally more expensive manner. Since such cases appear only rarely, the additional required computational effort is negligible in comparison to the standard one.

A single RK4 integration step per iteration is sufficient because the magnetic field is uniform within a cell. Respectively, the error of the RK4 method strongly scales with the Larmor radius  $\rho$  and can be brought below computer accuracy by a moderate grid refinement. Namely, in a tokamak geometry the error of a single step traversing the cell can be estimated as

$$\frac{\delta R(\Delta\tau)}{a} \sim \frac{\rho^3}{q^4 R^3} \Delta\varphi^5, \quad (13)$$

with  $R$ ,  $a$ ,  $q$  and  $\Delta\varphi$  denoting major radius, plasma radius, safety factor and toroidal cell length, respectively.

Due to the scaling of the error with  $\rho$ , for particles with mild energies (thermal electrons and ions) a less elaborate algorithm (*Gorilla Poly*) can be realized. By truncating the summation of eq. (11) at  $K = 2, 3$  or  $4$  one obtains approximate solutions of various orders in Larmor radius. With these solutions, equations for the dwell time  $\tau_d$  are algebraic equations which are solved analytically up to order  $K = 4$ , by finding the smallest positive root of

$$\mathbf{n}^\alpha \cdot \left( \mathbf{z}_0 + \sum_{k=1}^K \frac{\tau_d^k}{k!} (\hat{\mathbf{a}}^{k-1} \cdot \mathbf{b} + \hat{\mathbf{a}}^k \cdot \mathbf{z}_0) - \mathbf{z}^\alpha \right) = 0, \quad (14)$$

where  $\mathbf{n}^\alpha = (n_1^{(\alpha)}, n_2^{(\alpha)}, n_3^{(\alpha)}, 0)$  are face normals (see above) and  $\mathbf{z}^\alpha = (x_{(\alpha)}^1, x_{(\alpha)}^2, x_{(\alpha)}^3, 0)$ . Furthermore, by using the quadratic polynomial solution  $K = 2$  of eq. (14), the appropriate orbit intersection plane  $\alpha$  can be predicted for higher orders  $K = 3$  or  $4$ , which predominantly reduces the number of higher order root finding operations from four to one. In the numerical implementation, series (11) which contains matrix products is not directly evaluated as written above. Instead, various sub-products are preliminarily evaluated and stored for grid cells which minimizes the number of matrix products needed to be evaluated directly. The finite series solution (11) allows to analytically evaluate also various integrals over the dwell time needed for scoring of macroscopic plasma parameters in Monte Carlo procedures. In Appendix A, such integrals of  $v_{\parallel}$  and of  $v_{\perp}^2$  and  $v_{\parallel}^2$  are given, which respectively determine parallel plasma flow and components of the pressure tensor in Chew-Goldberger-

Low form essential for computation of equilibrium plasma currents.

### III. COLLISIONLESS GUIDING-CENTER ORBITS

#### A. Guiding-center orbits in an axisymmetric tokamak field

In this section the results of geometric orbit integration computed with *Gorilla* and the comparison to an exact orbit computed with a usual adaptive RK4/5 integrator are presented for an axisymmetric tokamak field configuration of ASDEX Upgrade (shot 26884 at 4300 ms) described in Ref. 33. The adaptive RK4/5 integrator requires high-order interpolation of electromagnetic fields with continuous derivatives, e.g. with help of 3D-splines, instead of continuous piecewise linear functions in case of the geometric integration method.

In axisymmetric configurations, the shape of the orbit is fully determined by three conservation laws,  $p_\varphi = \text{const.}$ ,  $J_\perp = \text{const.}$  and  $w = \text{const.}$ , where

$$p_\varphi = mv_\parallel \frac{B_\varphi}{B} + \frac{e}{c} A_\varphi \quad (15)$$

is canonical toroidal angular momentum. In geometric/symplectic numerical integration schemes this property is retained [19], which means that orbits must remain closed in the poloidal projection.

Due to the special formulation of eq. (2), where  $v_\parallel$  is purely a function of position, the perpendicular adiabatic invariant and the total energy are conserved naturally. By properly orienting the tetrahedra with respect to the symmetry direction, axisymmetry in case of 2D fields is exactly preserved upon linearization. Consequently, the canonical toroidal angular momentum remains invariant.

Fig. 3 depicts Poincaré plots ( $\varphi = 0$ ) of trapped thermal ion orbits making  $10^7$  toroidal turns which are integrated by different methods from the same starting conditions. Geometric integration using an iterative scheme with RK4 integration and Newton steps has been performed in cylindrical  $(R, \varphi, Z)$  and symmetry flux coordinates  $(s, \vartheta, \varphi)$  of Ref. 34 and is compared to the exact orbit. It can be seen, that the coarseness of the grid leads to slightly differently shaped orbits obtained in different coordinate systems, whereas the effect of the integration error (13) is negligible.

In Fig. 4 results of the geometric integration of a passing high energy ion (300 keV) using the polynomial series solution (11) are shown for the same axisymmetric geometry and compared

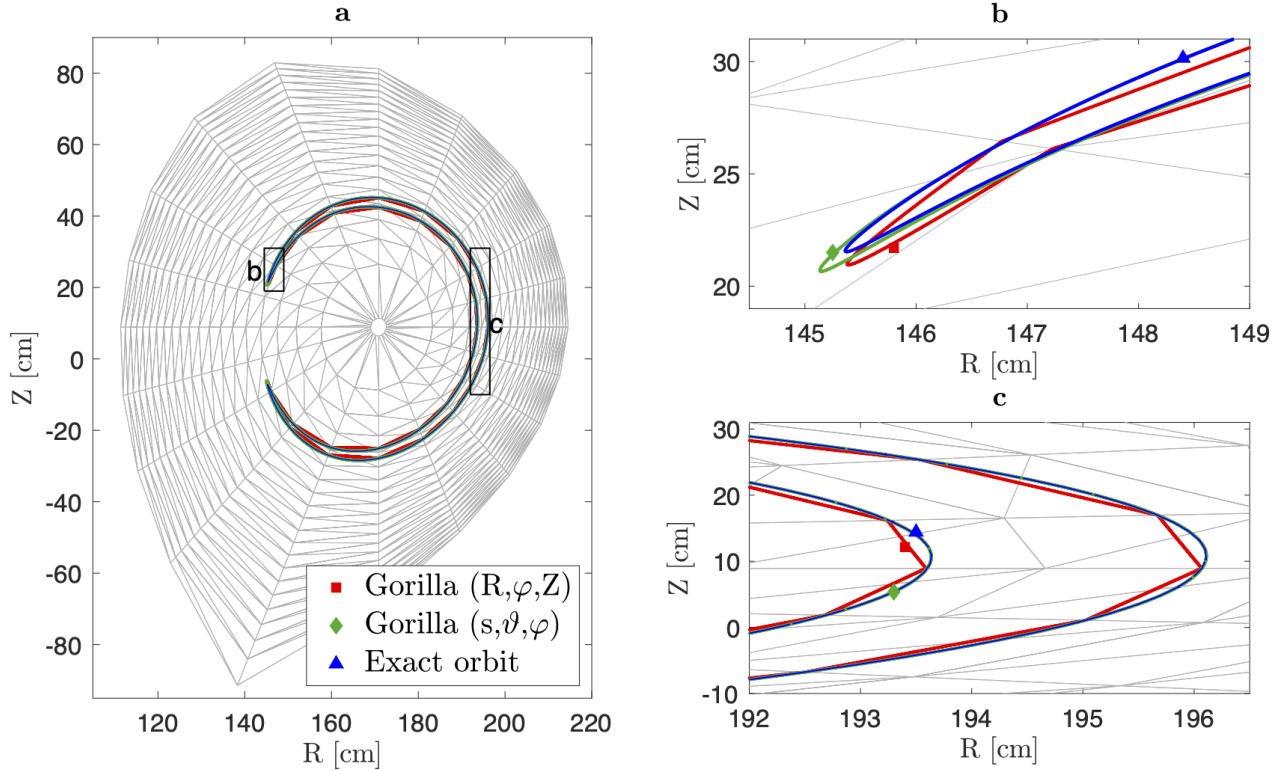


FIG. 3: (a) Poincaré plot ( $\varphi = 0, 10^7$  toroidal mappings) of a trapped 1.5 keV D ion in axisymmetric ASDEX Upgrade configuration with a tetrahedral grid size of  $20 \times 20 \times 20$ . Two-dimensional Poincaré sections of orbits obtained with different integration methods are indicated with markers: Exact orbit:  $\blacktriangle$ , 3D Geometric Integrator *Gorilla* with cylindrical coordinates:  $\blacksquare$ , *Gorilla* with symmetry flux coordinates:  $\blacklozenge$ . (b) and (c) are magnifications of the pertinent zones in (a).

to the exact orbit. Symmetry flux coordinates are used for the geometric integration, the results are then converted to cylindrical coordinates in the first plot (a). In general, the quartic polynomial solution ( $K = 4$ ) of ODE set (5) is equivalent to the numerical solution using Runge-Kutta 4, thus, the result of the latter is omitted in the figure. Moreover, it can be seen that even for high energy ions the series expansions of third and fourth order are already accurate enough in order to fulfill the condition  $p_\varphi = \text{const.}$  over  $10^6$  toroidal mappings. However, the second order series expansion shows a convective behavior, due to a systematic error from solving the ODE set (5). Nevertheless, for the electrons which have much smaller Larmor radii, the second order series expansion is sufficient.

To obtain the orbits of thermal ions shown in Fig. 5, uniformly distributed axisymmetric

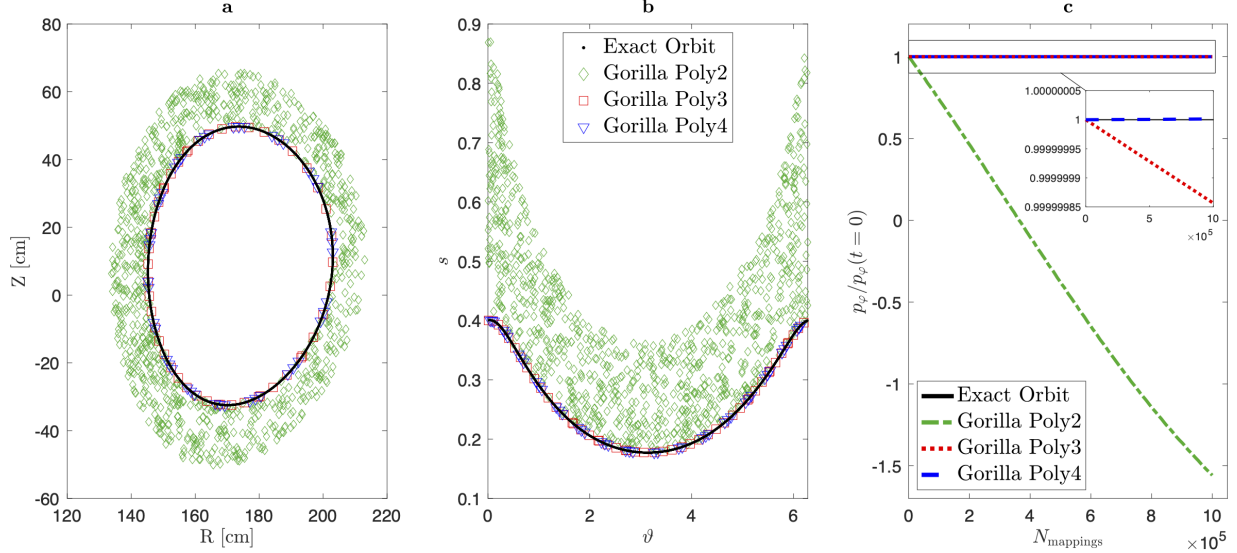


FIG. 4: (a & b) Poincaré plot ( $\varphi = 0$ ,  $10^6$  toroidal mappings) of a passing 300 keV D ion in axisymmetric ASDEX Upgrade configuration evaluated by the 3D Geometric Integrator *Gorilla* with the analytical solution in form of a polynomial series truncated at  $K = 2$  ( $\diamond$ ),  $K = 3$  ( $\square$ ) and  $K = 4$  ( $\nabla$ ) compared to the exact orbit ( $\bullet$ ). Cylindrical coordinates are used for the Poincaré plot in (a), whereas symmetry flux coordinates are used in (b).  
(c) Canonical toroidal angular momentum  $p_\varphi$  normalized to the value at  $t = 0$  is evaluated at the Poincaré sections in (a): Exact result (solid) is compared to polynomial series truncated at  $K = 2$  (dash-dotted),  $K = 3$  (dotted) and  $K = 4$  (dashed).

random noise ( $\xi = 0 \dots 1$ ) is added to the electrostatic potential  $\Phi^{\text{noisy}} = \Phi(1 + \epsilon_\Phi \xi)$ , to the vector potential  $A_k^{\text{noisy}} = A_k(1 + \epsilon_A \xi)$  and simultaneously to both quantities, respectively. Here,  $\epsilon$  is the relative magnitude of added noise. Even though relatively high noise (up to 30 %) is added, the orbits keep a similar shape in comparison with the unperturbed ones and remain closed in the poloidal projection, meaning the condition  $p_\varphi = \text{const.}$  is still fulfilled.

Therefore, the geometric integration method is suitable for self-consistent Monte Carlo modeling of 2D equilibrium plasma parameters and electromagnetic fields computed from those parameters. Further, it should be noted that the computational efficiency of the geometric integrator is not affected by the presence of small-scale noise. However, this would be the case for an adaptive RK4/5 integration in combination with high order smooth interpolation where the noise leads to small-scale oscillations.

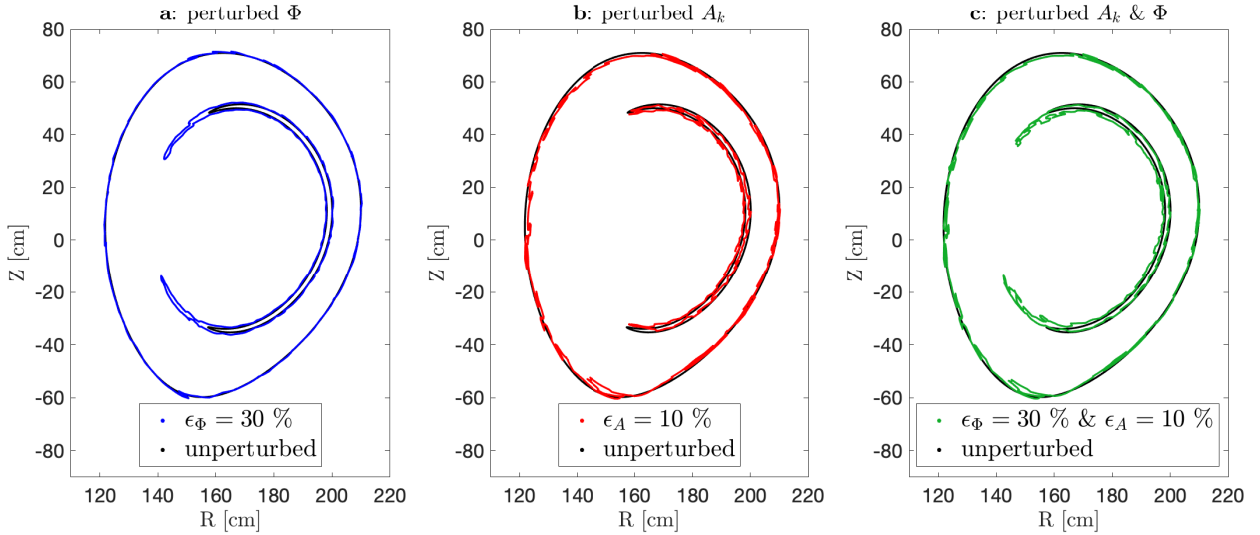


FIG. 5: Poincaré plot ( $\varphi = 0$ ) of trapped and passing 1.5 keV D ions in axisymmetric ASDEX Upgrade configuration with axisymmetric perturbation of electrostatic potential  $\Phi$  and vector potential  $A_k$ .

The Poincaré plot for unperturbed electromagnetic fields is depicted in black as a reference. Uniformly distributed axisymmetric random noise ( $\xi = 0 \dots 1$ ) is added in (a) to the electrostatic potential  $\Phi^{\text{noisy}} = \Phi(1 + \epsilon_\Phi \xi)$ , in (b) to the vector potential  $A_k^{\text{noisy}} = A_k(1 + \epsilon_A \xi)$  and in (c) to both quantities.

The Poincaré plots ( $\varphi = 0$ ) of Fig. 6 (a) & (b) correspond to a trapped high energy ion (300 keV), where the orbits are integrated using the polynomial series expansion in several orders and compared to the exact orbit. Again, symmetry flux coordinates are used for the geometric integration, the results are then converted to cylindrical coordinates in the first plot (a). Despite the same starting conditions of all orbits, the magnification in (b) clearly depicts differences in the shape of the orbits caused by a finite grid size ( $100 \times 100 \times 100$ ) and different orders of the series expansion.

Fig. 6 (c) shows the corresponding time evolution of the parallel adiabatic invariant  $J_{\parallel}$ , which is defined by an integral over the distance  $l$  passed along the field line during a single bounce period  $t_b$  by a trapped particle as follows,

$$J_{\parallel} = m \oint v_{\parallel} dl = m \int_0^{t_b} v_{\parallel}^2(t) dt. \quad (16)$$

For an exact orbit,  $J_{\parallel}$  is a conserved quantity. Symplectic orbit integration does not lead to an error accumulation in the invariants of motion [19], while systematic changes can only arise from numerical errors in solving the ODE. Even for high energy ions the series expansions of third and fourth order are already accurate enough in order to fulfill the condition

$J_{\parallel} = \text{const.}$  for  $10^6$  bounce periods. Hence, in an axisymmetric configuration excellent long-term orbit dynamic is demonstrated by the geometric orbit integration method, as long as the ODE set (5) is solved accurately.

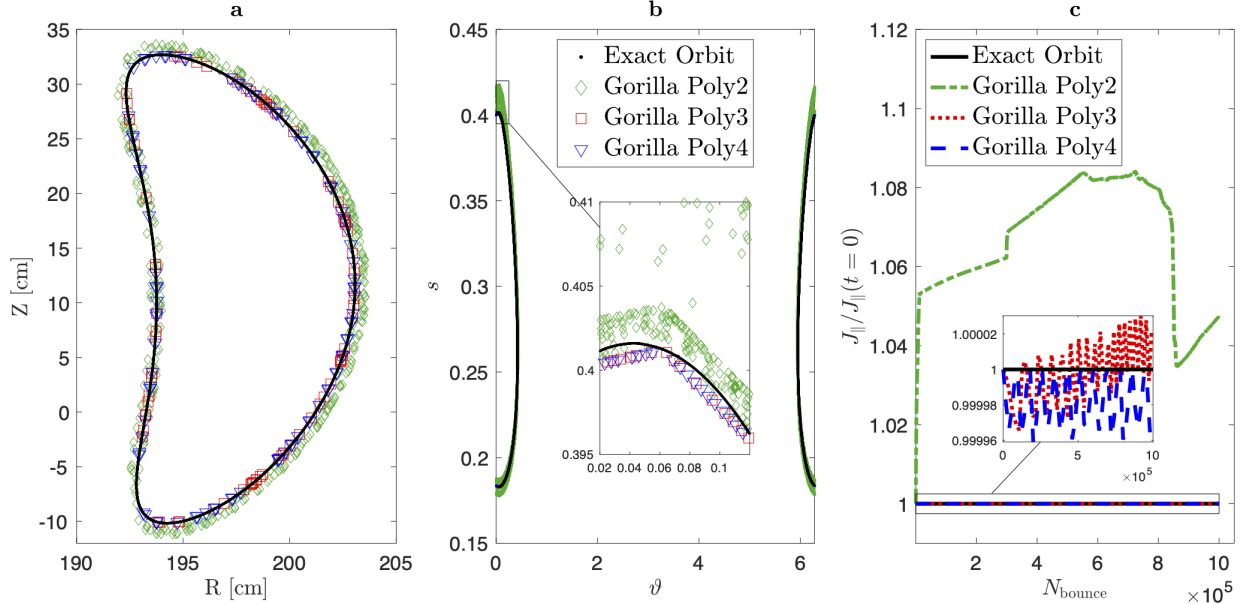


FIG. 6: (a & b) Poincaré plot ( $\varphi = 0$ ,  $10^6$  bounce periods) of a trapped 300 keV D ion in axisymmetric ASDEX Upgrade configuration evaluated by the 3D Geometric Integrator *Gorilla* with the analytical solution in form of a polynomial series truncated at  $K = 2$  ( $\diamond$ ),  $K = 3$  ( $\square$ ) and  $K = 4$  ( $\nabla$ ) compared to the exact orbit ( $\bullet$ ). Cylindrical coordinates are used for the Poincaré plot in (a), whereas symmetry flux coordinates are used in (b). The magnification in (b) shows the banana tip and clearly depicts the difference of polynomial orders.

(c) The parallel adiabatic invariant  $J_{\parallel}$  normalized to the value at  $t = 0$  is depicted for  $10^6$  bounce periods: Exact result (solid) is compared to polynomial series truncated at  $K = 2$  (dash-dotted),  $K = 3$  (dotted) and  $K = 4$  (dashed).

## B. Guiding-center orbits in three-dimensional fields

It can be seen from Eqs. (5) and (6) that in the field line limit  $\omega_c \rightarrow \infty$  guiding-center orbits are straight within spatial cells and magnetic field lines are represented by polygonal chains, respectively. In case of 3D magnetic fields described in non-aligned spatial coordinates, the existence of embedded KAM surfaces is not obvious for such an approximate representation

of the field even in case these surfaces exist in the exact system. In order to study artificial chaos induced by the linearization, geometric orbit integration has been performed for low energy particles with negligible FLR effects in symmetry flux coordinates  $(s, \vartheta, \varphi)$  associated with the axisymmetric tokamak field of the previous section with a harmonic perturbation added to the toroidal co-variant component of the axisymmetric vector potential,

$$A_\varphi = \psi_{\text{pol}}(s)(1 + \varepsilon_M \cos(m_0\vartheta + n_0\varphi)). \quad (17)$$

The harmonic indices  $m_0 = n_0 = 2$  used in the testing correspond to a non-resonant perturbation which leads only to a corrugation of the magnetic surfaces such that they are not aligned with the coordinate surfaces  $s = \text{const.}$  anymore.

In Fig. 7, Poincaré plots of magnetic field lines obtained by the geometric integration method for this perturbed configuration are shown at the cross section  $\varphi = 0$  together with a cross section of one exact corrugated flux surface. It can be seen that the orbits from the geometric integrator become more chaotic with increasing perturbation amplitude  $\varepsilon_M$ . Diffusive behavior of orbits can be characterized by the variance of the normalized toroidal flux  $s$ , accumulated over the time for the ensemble of test particles starting from the same perturbed flux surface. This variance is described by the magnetic field line diffusion coefficient  $D_M^{ss}$  as  $\langle \delta s^2 \rangle = 2D_M^{ss}N$  where  $N$  is the number of toroidal orbit turns. The effective diffusion coefficient  $D_M^{ss}$  computed from the orbits has a strong inverse scaling with poloidal  $N_\vartheta$  and toroidal  $N_\varphi$  grid sizes and, furthermore, shows in general a small magnitude of diffusion even at coarse angular grid resolution. E.g., at an angular grid size of  $N_\vartheta = N_\varphi = 30$  the effective diffusion coefficient  $D_M^{ss}$  is in the order of  $10^{-13}$ ,  $10^{-11}$  and  $10^{-9}$  for relative perturbation amplitudes of  $\varepsilon_M = 1\%$ ,  $3\%$  and  $10\%$ , respectively. This level of field line diffusion is roughly five orders of magnitude smaller than observed for the initial version of the code<sup>29</sup>, and, in the worst case of  $\varepsilon_M = 0.1$ , results in stochastic diffusion of electrons with the coefficient  $D_\perp \sim D_M^{ss}v_\parallel r^2/R \sim 100 \text{ cm}^2\text{s}^{-1}$ . For smaller  $\varepsilon_M$  values of the typical order for external magnetic perturbations in tokamaks this numerical diffusion is below the level of classical electron diffusion and, therefore, can be safely ignored.

In case of field aligned coordinates, chaotization of passing orbits (lines of force of the effective field  $\mathbf{B}^*$ ) can only be caused by the cross-field drift. Such a case is tested below for a strong violation of axial symmetry using as an example the stellarator field configuration described in Ref. 31, namely, a quasi-isodynamic reactor-scale device with five toroidal field

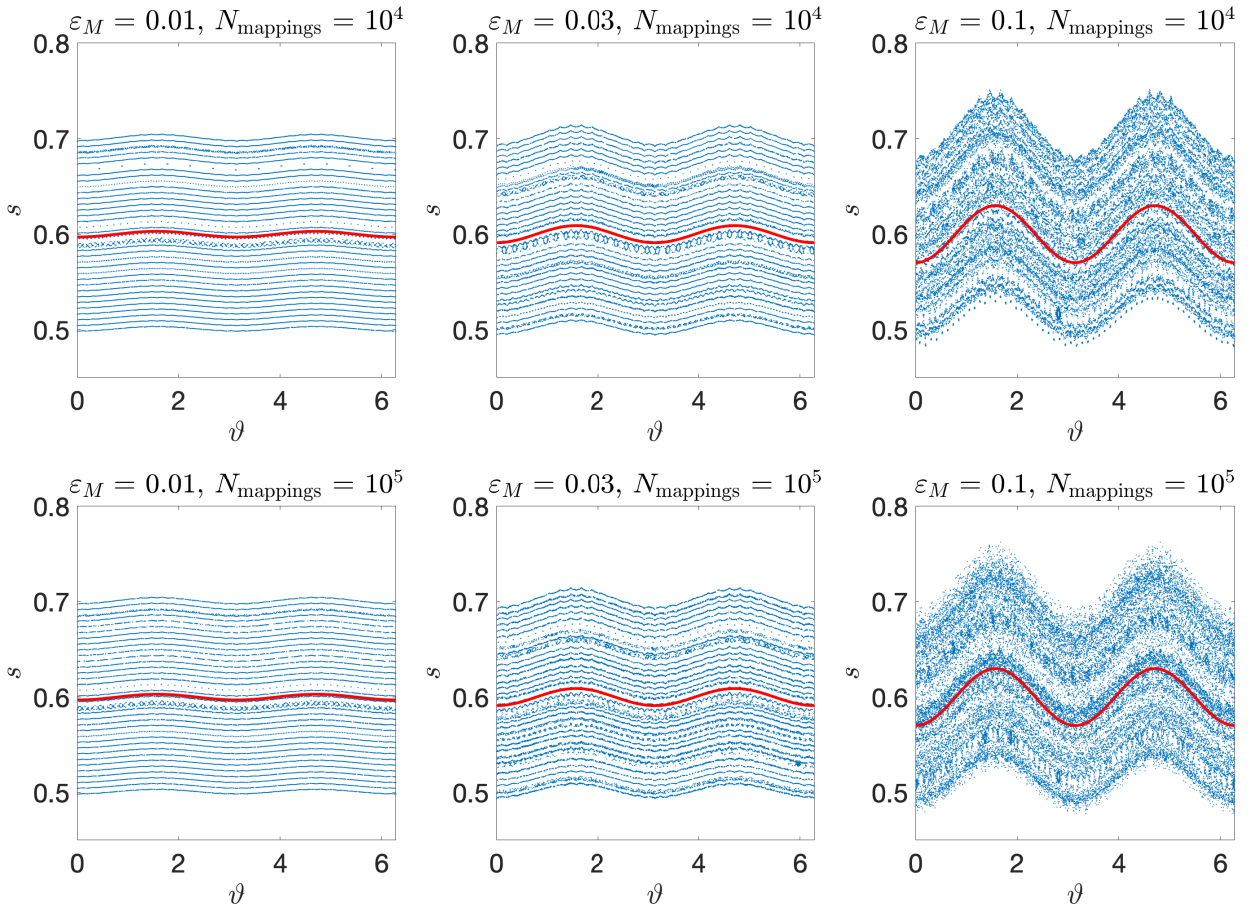


FIG. 7: Poincaré plots of the orbits in zero Larmor radius limit (field lines) for  $10^4$  (upper raw) and  $10^5$  (lower raw) toroidal mappings and various perturbation amplitudes indicated in the titles. Orbits start at 34 equidistant flux surfaces between  $s = 0.5$  and  $s = 0.7$  and are evaluated by *Gorilla* with polynomial series truncated at  $K = 2$  and angular grid size of  $N_\vartheta = N_\varphi = 30$ . Similar results are achieved for angular grid size with incommensurable dimensions, e.g.  $N_\vartheta = 29, N_\varphi = 31$ . Solid line shows a cross-section of one exact corrugated flux surface.

periods and major radius of 25 m. Here the magnetic field has been normalized so that its modulus averaged over Boozer coordinate angles on the starting surface is  $B_{00} = 5$  T. Guiding-center orbits were computed with the geometric integration method in symmetry flux coordinates for strongly passing electrons and ions with  $v_\parallel/v = 0.9$  at the starting point on the flux surface  $s = 0.6$  with an energy of 3 keV. The numerical diffusion observed for a rather coarse angular grid with the size  $N_\vartheta = N_\varphi = 30$  is roughly seven orders of magnitude

smaller than the minimum level of the neoclassical mono-energetic diffusion coefficient  $D_{11}$  evaluated in section IV for the same device with particles of the same energy.

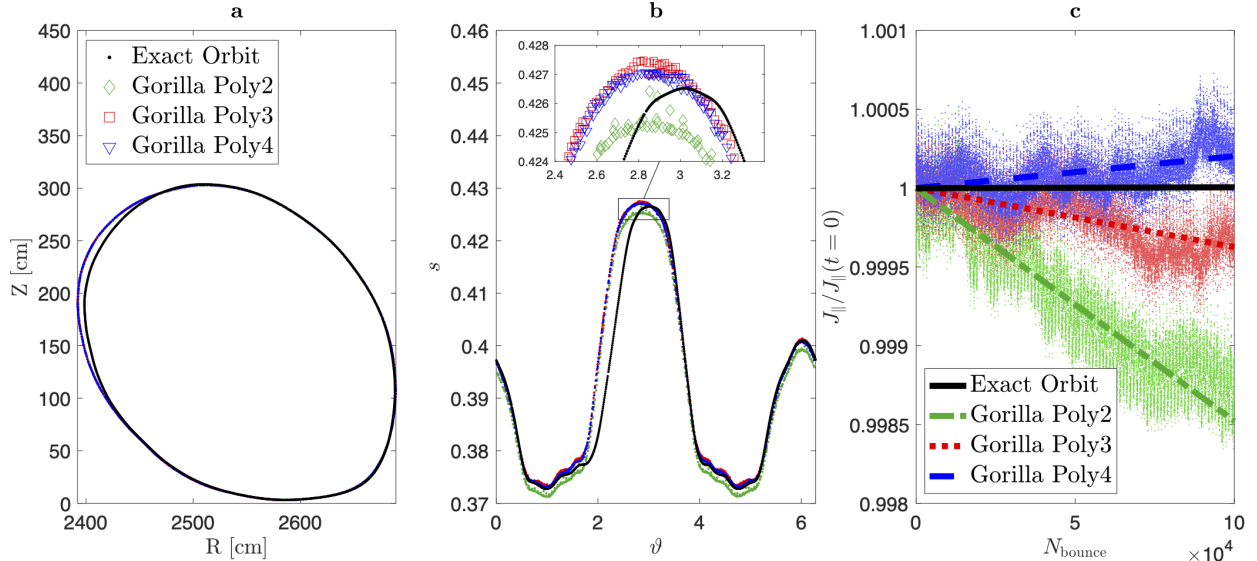


FIG. 8: (a & b) Poloidal projection of Poincaré sections at  $v_{\parallel} = 0$  switching sign from  $-$  to  $+$  of a trapped 3 keV D ion in 3D stellarator field configuration. Orbits evaluated by *Gorilla* with the analytical solution in form of a polynomial series truncated at  $K = 2$  ( $\diamond$ ),  $K = 3$  ( $\square$ ) and  $K = 4$  ( $\nabla$ ) are compared to the exact orbit ( $\bullet$ ). Poincaré plot is depicted in cylindrical coordinates (a) and symmetry flux coordinates (b). (c) Evolution of the parallel adiabatic invariant  $J_{\parallel}$  normalized to the value at  $t = 0$  in (a) and (b) over  $10^5$  bounce times. Lines in (c) represent linear fits to the  $J_{\parallel}$  data points: Exact result (solid) is compared to polynomial series truncated at  $K = 2$  (dash-dotted),  $K = 3$  (dotted) and  $K = 4$  (dashed).

For the visualization of a trapped particle orbit, we use orbit footprints on Poincaré sections defined by the condition  $v_{\parallel}(\tau) = 0$ , i.e. phase space hypersurfaces containing orbit turning points. Out of two kinds of these surfaces, those are chosen where the sign of  $v_{\parallel}$  changes from negative to positive. Fig. 8 depicts a poloidal projection of orbit footprints corresponding to a trapped ion with an energy of 3 keV. The orbits have been integrated in symmetry flux coordinates using the polynomial series expansion in several orders and compared to the exact orbit computed with an adaptive RK4/5 integrator. Further, the poloidal coordinates of the footprints have also been converted to cylindrical coordinates and visualized in both coordinate systems, respectively. Despite the same starting conditions of all orbits, the magnification in (b) clearly depicts differences in the shape of the orbits caused by a finite grid size ( $100 \times 100 \times 100$ ) and different orders of the series expansion.

In contrast to the axisymmetric tokamak field of the previous section, the parallel adiabatic invariant  $J_{\parallel}$  is not an exact invariant in a stellarator. Nevertheless, it should be well preserved as long as the trapped orbit stays within the same class (traverses the same number of field minima over its bounce period) which is the case here. Fig. 8 (c) shows the time evolution of  $J_{\parallel}$  for  $10^5$  bounce periods of the corresponding orbits. It can be seen that the results for the exact orbit shows no visible deviation for this configuration. Furthermore, the finite grid size used in the geometric orbit computation does not lead to a significant error accumulation even for the order  $K = 2$  which is naturally the fastest with respect to CPU time.

#### IV. MONTE CARLO EVALUATION OF NEOCLASSICAL TRANSPORT COEFFICIENTS, PERFORMANCE BENCHMARK

Evaluation of neoclassical transport coefficients using the Monte Carlo method<sup>1,2</sup> is widely used for stellarators and tokamaks with 3D perturbations of the magnetic field<sup>4–9,35</sup>. An advantage of this method in its original, full- $f$  form is the use of test particle guiding-center orbits without requiring model simplifications needed in (more efficient) local approaches. Therefore Monte Carlo methods provide an unbiased reference point in cases where those simplifications affect the transport such as for regimes with significant role of the tangential magnetic drift<sup>36,37</sup>. An obvious disadvantage is that for realistic magnetic configurations Monte Carlo methods are CPU-intensive with most of the CPU time spent for the integration of the guiding-center motion. The application of the proposed geometric integration method for this purpose instead of the usual Runge-Kutta method results in a visible speed-up of the computations without significantly biasing the results. Here, this application is made for benchmarking purposes assuming that the inaccuracies in orbit integration which are tolerable in computations of transport coefficients are also tolerable in global modelling of macroscopic plasma parameters.

The proposed orbit integration method is applied within a standard Monte Carlo algorithm<sup>1</sup> using the Lorentz collision model for the evaluation of the mono-energetic radial diffusion coefficient  $D_{11}$ . The latter is determined via the average square deviation of the normalized toroidal flux  $s$  from its starting value  $s_0$  as follows,

$$D_{11} = \frac{1}{2t} \langle (s(t) - s_0)^2 \rangle. \quad (18)$$

Here, angle brackets  $\langle \dots \rangle$  denote an ensemble average,  $s(0) = s_0$ , and the test particle tracing time  $t$  is chosen to be larger than the local distribution function relaxation time  $\tau_{\text{rel}}$  and smaller than the radial transport time,  $t = 10\tau_{\text{rel}}$ . A Monte Carlo collision operator identical to that of Ref. 1 is applied here in-between constant collisionless orbit integration steps  $\Delta t$ . These steps are small enough compared to the typical bounce time  $\tau_b$  and collision time  $\tau_c$ ,

$$\Delta t = \min \left( \frac{\tau_b}{20}, \frac{\tau_c}{20} \right). \quad (19)$$

Here,  $\tau_c = 1/\nu$  and  $\tau_b = 2\pi R_0/(vN_{\text{tor.}})$  with  $\nu$ ,  $R_0$ ,  $v$  and  $N_{\text{tor}}$  denoting collisional deflection frequency, major radius, particle velocity and number of toroidal field periods, respectively. The relaxation time  $\tau_{\text{rel}}$  is determined as the largest of  $\tau_c$  and  $\tau_b^2/\tau_c$ .

In the present example, the mono-energetic radial diffusion coefficient has been evaluated for the quasi-isodynamic stellarator configuration<sup>31</sup> used also for collisionless orbits in section III B. Guiding-center orbits were computed with the geometric integration method in symmetry flux coordinates using polynomial series solutions of various orders  $K$ . The grid size  $N_s \times N_\theta \times N_\varphi = 100 \times 60 \times 60$  was selected to be appropriate to minimize the numerical diffusion (see the previous section.) In a reference computation, guiding-center equations (1) in symmetry flux variables with electromagnetic field interpolated by 3D cubic splines were integrated by an adaptive RK4/5 integrator. In order to minimize statistical errors, computations have been performed for a large ensemble size of 10000 particles.

The results for  $D_{11}$  computed for 3 keV electrons and ions at  $s_0 = 0.6$  are presented in Fig. 9. Values of radial electric field  $E_r$  and deflection frequency  $\nu$ , which determine transport regimes, are respectively characterized here by two dimensionless parameters<sup>38</sup>, Mach number  $v_E^* = cE_r/(vB_0)$  and collisionality  $\nu^* = (R_0\nu)/(\iota v)$ , where  $\iota$  is the rotational transform. For the ions, in addition to the  $\mathbf{E} \times \mathbf{B}$  rotation, also the tangential magnetic drift plays a significant role which can be seen from the shift of the  $D_{11}$  maximum on  $v_E^*$  dependence. The results of geometric integration stay in agreement with the reference computation within the 95 % confidence interval in all cases even for the lowest order polynomial solution  $K = 2$ . Therefore, as shown below, a significant gain in the computation time can be obtained in this kind of calculations.

Moreover, we compare the performance and scaling for parallel computation of guiding-center orbits using the geometric orbit integration method with computations using standard reference integrators (RK4 and adaptive RK4/5). For this, different integrators have

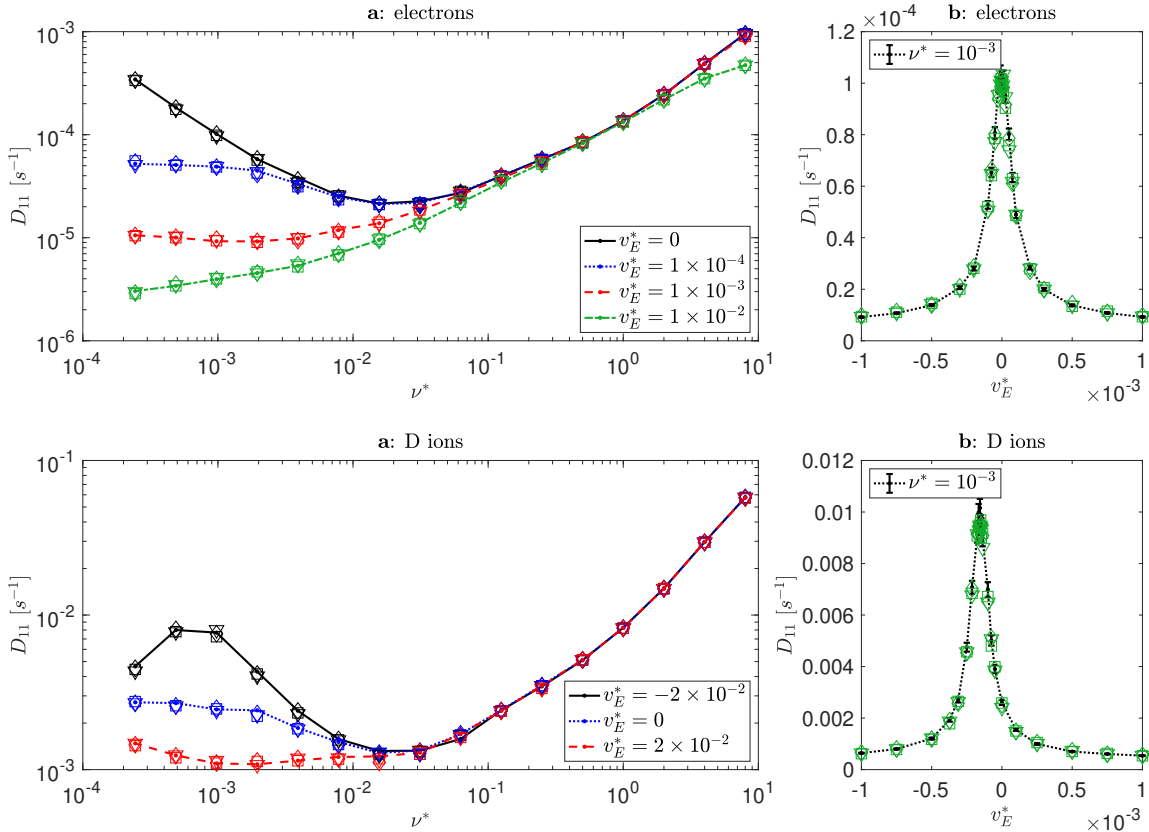


FIG. 9: Mono-energetic radial diffusion coefficients  $D_{11}$  for electrons (top) and deuterium ions (bottom) as functions of (a) normalized collisionality  $\nu^*$  and (b) Mach number  $v_E^*$ . Lines of various styles (see the legends) - reference computation, markers - results of geometric integration with polynomial solution of the order  $K$  for  $K = 2$  ( $\diamond$ ),  $K = 3$  ( $\square$ ) and  $K = 4$  ( $\nabla$ ). Error bars indicate 95 % confidence interval.

been used within  $D_{11}$  computation described above for a particular choice of dimensionless parameters,  $v_E^* = 10^{-3}$  and  $\nu^* = 10^{-3}$ , and an increased ensemble size of 30000 test particles. The numerical experiment has been performed on a single node of the COBRA cluster of MPCDF with 40 CPU cores (Intel Xeon Gold 6126) running 80 concurrent threads with hyperthreading.

The reference value for the transport coefficient,  $D_{11,\text{ref}}$ , and the reference CPU time are obtained by orbit integration with an adaptive RK4/5 integrator with a relative tolerance of  $10^{-9}$ . The accuracy of the  $D_{11}$  evaluation using different computation parameter settings is represented by the relative error  $\delta D_{11}/D_{11,\text{ref}}$  where  $\delta D_{11} = |D_{11} - D_{11,\text{ref}}|$ . The CPU time purely used for orbit integration serves as a measure for the computational effort of the

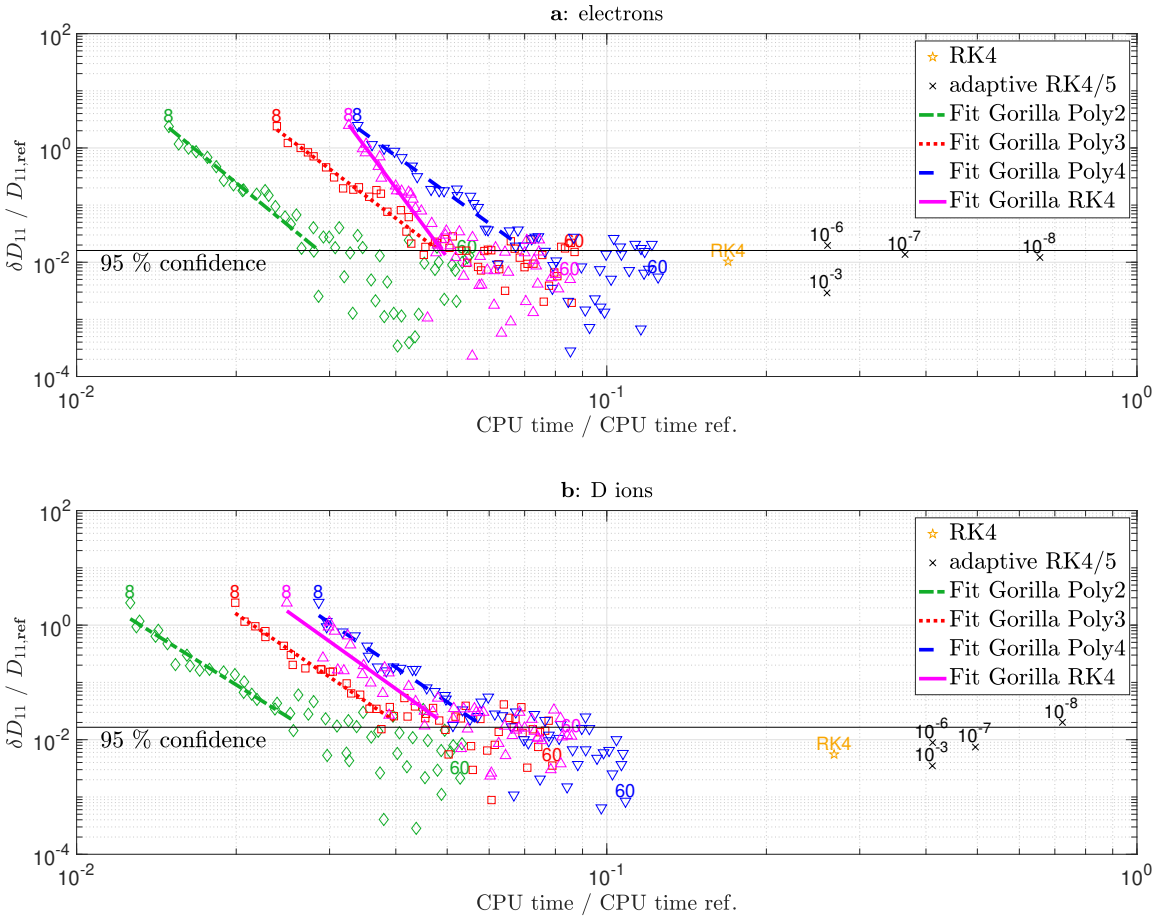


FIG. 10: Relative error of mono-energetic radial transport coefficient  $D_{11}$  of electrons (top) and D ions (bottom) vs. relative CPU time. Compared orbit integration methods are: Runge-Kutta 4 ( $\star$ ), Adaptive RK4/5 with various relative errors indicated in the plot ( $\times$ ), geometric integration with polynomial solution (*Gorilla Poly*) of the order  $K = 2$  ( $\diamond$ ),  $K = 3$  ( $\square$ ) and  $K = 4$  ( $\nabla$ ), and with RK4 solution (*Gorilla RK4*,  $\triangle$ ). Fits of results are depicted with lines according to the legend. Random error of the reference result,  $D_{11,\text{ref}}$ , is depicted as a horizontal line limiting its 95 % confidence interval.

methods. This given CPU time does not contain any overhead operations, e.g. the construction of the grid, generation of random numbers for pitch-angle scattering and computation of  $D_{11}$  by evaluating Eq. 18 with the help of a least-squares regression.

Fig. 10 shows the relative error of the mono-energetic radial transport coefficient versus the relative CPU time of computations using the geometric orbit integration method with the polynomial series solution of various orders, *Gorilla Poly*, and the iterative scheme with

RK4 integration and Newton steps, *Gorilla RK4*. Accuracy and CPU time of geometric orbit integrations have been varied by mutually changing the angular grid size  $N_\theta \times N_\varphi$  from  $8 \times 8$  to  $60 \times 60$  while keeping the radial grid size constant at  $N_s = 100$ . In the stellarator configuration of Ref. 31 used here, the number of toroidal harmonic modes per field period is 14, leading to a minimum toroidal grid size  $N_\varphi = 28$  in order to satisfy the Nyquist-Shannon sampling theorem<sup>39,40</sup>. Therefore, regression lines are drawn for the range of data points with grid sizes from  $8 \times 8$  until  $28 \times 28$ , clearly showing a convergent behavior of  $D_{11}$  with increasing grid refinement. Furthermore, the adaptive RK4/5 integration is additionally performed with relative tolerances of  $10^{-3}$ ,  $10^{-6}$ ,  $10^{-7}$  and  $10^{-8}$ , respectively. Note that the computational speed of the adaptive RK4/5 integration with a relative tolerance of  $10^{-6}$  cannot be increased by higher relative tolerances, e.g.  $10^{-3}$ , since the macroscopic Monte Carlo time step,  $\Delta t$  Eq. (19), is already elapsed within a single RK4/5 step with sufficient accuracy. Hence, also the non-adaptive Runge-Kutta 4 method is tested, which naturally needs one field evaluation less per time step than RK4/5. In all cases, the relative error of RK4/5 and Runge-Kutta 4 results is determined here mainly by statistical deviations, with a random error dominating the bias.

Besides statistical errors due to Monte Carlo sampling, a limit for capturing all toroidal and poloidal field harmonics is given by a minimum grid size of two points per period due to the Nyquist–Shannon sampling theorem. Fig. 10 visibly shows that statistical fluctuations already dominate the bias of all variants of the geometric integration method above this sampling threshold, despite the large ensemble size of 30000 particles. To avoid possible sampling artifacts at even higher higher particle count, we consider the geometric orbit integration method at the toroidal grid size  $N_\varphi$  of at minimum twice the number of toroidal modes in the magnetic field configurations. The variant with the polynomial series solution truncated at  $K = 2$  (*Gorilla Poly 2*) at this grid resolution can be considered the fastest sufficiently accurate tested method to compute  $D_{11}$  for thermal ions and electrons. In case of D ions with an energy of 3 keV this method is one order of magnitude faster than the Runge-Kutta 4 integrator which is the fastest reference method.

## V. SUMMARY AND OUTLOOK

A geometric integration method for guiding-center orbits in general three-dimensional toroidal fields has been developed, implemented and presented here. This orbit integration procedure is based on a representation of the electromagnetic field by continuous piecewise linear functions using a spatial mesh. Collisionless particle orbits in real space and magnetic coordinates and their respective invariants of motion have been studied in detail for axisymmetric and non-axisymmetric geometries. Due to the special formulation of the guiding-center equations, the magnetic moment and the total energy are conserved naturally. In case of toroidal axisymmetry the canonical toroidal angular momentum is accurately preserved by the geometric method, as well as the parallel invariant. Thus, the property of such systems to ideally confine the orbits is retained. For passing orbits in 3D fields, however, the piecewise linearization of the electromagnetic field introduces some artificial chaotic diffusion which, nevertheless, could be made negligibly small by spatial grid refinement. For trapped orbits in 3D fields, the approximate conservation of the parallel adiabatic invariant is not violated by significant error accumulation.

To assess the method's performance, the mono-energetic radial transport coefficient,  $D_{11}$ , which gives a main contribution to neoclassical transport, has been evaluated for a quasi-isodynamic reactor-scale stellarator field<sup>31</sup> using the Monte Carlo method. For both, electrons and ions, the results obtained by geometric orbit integration are in good agreement with the results of adaptive RK4/5 integration with usual spline interpolation of electromagnetic fields. In the performance benchmark, we observe that the geometric orbit integration method with the polynomial series solution truncated at  $K = 2$  is the fastest sufficiently accurate tested method to compute  $D_{11}$ . For the case of D ions with an energy of 3 keV the guiding-center orbit integration is one order of magnitude faster than 4th order Runge-Kutta integration in splined fields.

For the application in global kinetic computations no extra effort is needed to obtain dwell times within spatial grid cells as these are computed automatically in the present approach. Additionally, integrals of velocity powers over these dwell times are available as analytical expressions. The latter quantities are required for statistical scoring of orbits in Monte Carlo computations of macroscopic parameters, such as plasma response currents and charges caused by external non-axisymmetric perturbations in tokamaks or parameters of the edge

plasma in devices with 3D field geometry. Moreover, similarly to the geometric integrator for axisymmetric two-dimensional fields described in Ref. 30, the presented method is less sensitive to noise in the electromagnetic field than procedures relying upon high order polynomial interpolation. These characteristics suggest additional overall performance enhancements in both numerical stability and computational efficiency, when the geometric orbit integration is applied to kinetic modeling.

Finally, it should be mentioned that the method facilitates the coupling with kinetic neutral particle codes like EIRENE<sup>41</sup>, where one needs to model particle conversion into neutrals and back with plasma and neutral particles described in different coordinate systems. Necessary transformation of coordinates does not require solving any implicit dependencies (nonlinear equations), since that is a linear operation in this approach and therefore intrinsically fast.

## ACKNOWLEDGEMENTS

The authors would like to thank Michael Drevlak, Markus Meisterhofer, Artem Savchenko and Harry Mynick for respectively providing stellarator field configurations, Fortran advice, a tool for non-linear coordinate transformations and a tutorial for neoclassical transport in 3D systems, as well as Martin Heyn, Philipp Ulbl, Rico Buchholz, Patrick Lainer and Markus Richter for useful discussions. This work has been carried out within the framework of the EUROfusion Consortium and has received funding from the Euratom research and training programmes 2014–2018 and 2019–2020 under grant agreement no. 633053. The views and opinions expressed herein do not necessarily reflect those of the European Commission. The study was supported by the Reduced Complexity Models grant number ZT-I-0010 funded by the Helmholtz Association of German Research Centers. Support from NAWI Graz, and from the OeAD under the WTZ grant agreement with Ukraine No. UA 04/2017 is gratefully acknowledged.

## Appendix A: Analytical integrals of velocity powers over the dwell time

In this section it is presented how analytical expressions for the dwell time integrals of  $v_{\perp}^2$ ,  $v_{\parallel}$  and  $v_{\parallel}^2$  can be obtained. Furthermore, the latter quantity is exemplary given as an explicit expression.

We start with the exact polynomial series solution of ODE set (5)

$$\mathbf{z} = \mathbf{z}_0 + \sum_{k=1}^{\infty} \frac{\tau^k}{k!} (\hat{\mathbf{a}}^{k-1} \cdot \mathbf{b} + \hat{\mathbf{a}}^k \cdot \mathbf{z}_0), \quad (\text{A1})$$

already given in Eq. (11). For the parallel velocity  $v_{\parallel} = z^4$  this series can be written in form of a shifted exponential function

$$v_{\parallel}(\tau) = e^{\alpha\tau} \left( v_{\parallel,0} + \frac{\beta}{\alpha} \right) - \frac{\beta}{\alpha}, \quad (\text{A2})$$

where  $\alpha$ ,  $\beta$  and  $v_{\parallel,0}$  stand for the matrix element  $a_{44}$ , the vector component  $b^4$  and the initial value for the parallel velocity at the cell entry, respectively. After squaring Eq. (A2), one can perform a Taylor series expansion of the orbit parameter up to the 4<sup>th</sup> order,

$$\begin{aligned} v_{\parallel}^2(\tau) \approx & v_{\parallel,0}^2 + \tau(2\beta v_{\parallel,0} + 2\alpha v_{\parallel,0}^2) + \tau^2 (\beta^2 + 3\alpha\beta v_{\parallel,0} + 2\alpha^2 v_{\parallel,0}^2) \\ & + \tau^3 \left( \alpha\beta^2 + \frac{7}{3}\alpha^2\beta v_{\parallel,0} + \frac{4}{3}\alpha^3 v_{\parallel,0}^2 \right) + \frac{1}{12}\tau^4 (7\alpha^2\beta^2 + 15\alpha^3\beta v_{\parallel,0} + 8\alpha^4 v_{\parallel,0}^2). \end{aligned} \quad (\text{A3})$$

This is the highest order, where an algebraic expression of the dwell time  $t_d$  to pass a cell can be found. In order to obtain the dwell time integral of  $v_{\parallel}^2$ , its polynomial representation can simply be integrated

$$\begin{aligned} \int_0^{t_d} v_{\parallel}^2(t) dt \approx & C \left( \tau_d v_{\parallel,0}^2 + \frac{1}{2}\tau_d^2 (2\beta v_{\parallel,0} + 2\alpha v_{\parallel,0}^2) + \frac{1}{3}\tau_d^3 (\beta^2 + 3\alpha\beta v_{\parallel,0} + 2\alpha^2 v_{\parallel,0}^2) \right. \\ & \left. + \frac{1}{4}\tau_d^4 \left( \alpha\beta^2 + \frac{7}{3}\alpha^2\beta v_{\parallel,0} + \frac{4}{3}\alpha^3 v_{\parallel,0}^2 \right) + \frac{1}{60}\tau_d^5 (7\alpha^2\beta^2 + 15\alpha^3\beta v_{\parallel,0} + 8\alpha^4 v_{\parallel,0}^2) \right), \end{aligned} \quad (\text{A4})$$

where  $C = dt/d\tau = B_{\parallel}^* \sqrt{g} = \text{const.}$  within the cell.

Clearly, the dwell time integral of  $v_{\parallel}$  requires to omit squaring of Eq. (A2) and to proceed straightforwardly in the same manner.

Moreover, the squared perpendicular velocity  $v_{\perp}^2$  is purely a function of position inside a tetrahedral cell due to its proportionality with the cyclotron frequency,  $v_{\perp}^2 = 2\omega_c \frac{J_{\perp}}{m}$ , which is a piecewise linear function of position in the geometric orbit integration formulation. Thus, the dwell time integral of  $v_{\perp}^2$  is obtained via an integral along the orbit which can easily be computed by using its polynomial representation given in Eq. (A1).

## REFERENCES

<sup>1</sup>A. H. Boozer and G. Kuo-Petravic, Phys. Fluids **24**, 851 (1981).

<sup>2</sup>W. Lotz and J. Nührenberg, Phys. Fluids **31**, 2984 (1988).

<sup>3</sup>J. A. Heikkinen, T. P. Kiviniemi, T. Kurki-Suonio, A. G. Peeters, and S. K. Sipilä, Journal of Computational Physics **173**, 527 (2001).

<sup>4</sup>A. Wakasa, S. Murakami, and S. Oikawa, Plasma and Fusion Research **3**, S1030 (2008).

<sup>5</sup>V. Tribaldos, Phys. Plasmas **8**, 1229 (2001).

<sup>6</sup>M. Y. Isaev, S. Brunner, W. Cooper, T. Tran, A. Bergmann, C. Beidler, J. Geiger, H. Maassberg, J. Nührenberg, and M. Schmidt, Fusion Sci. Technol. **50**, 440 (2006).

<sup>7</sup>K. Allmaier, S. V. Kasilov, W. Kernbichler, and G. O. Leitold, Phys. Plasmas **15**, 072512 (2008).

<sup>8</sup>S. Satake, J.-K. Park, H. Sugama, and R. Kanno, Phys. Rev. Letters **107**, 055001 (2011).

<sup>9</sup>D. Pfefferlé, W. A. Cooper, J. P. Graves, and C. Misev, Comput. Phys. Commun. **185**, 3127 (2014).

<sup>10</sup>S. Jollet, A. Bottino, P. Angelino, R. Hatzky, T. M. Tran, B. F. Mcmillan, O. Sauter, K. Appert, Y. Idomura, and L. Villard, Comput. Phys. Commun. **177**, 409 (2007).

<sup>11</sup>A. Mishchenko, R. Hatzky, and A. Könies, Phys. Plasmas **15**, 1904 (2008).

<sup>12</sup>R. Hager and C. S. Chang, Physics of Plasmas **23**, 042503 (2016).

<sup>13</sup>S. Ku, C. S. Chang, R. Hager, R. M. Churchill, G. R. Tynan, I. Cziegler, M. Greenwald, J. Hughes, S. E. Parker, M. F. Adams, E. D'Azevedo, and P. Worley, Physics of Plasmas **25**, 056107 (2018).

<sup>14</sup>C. G. Albert, M. F. Heyn, S. V. Kasilov, W. Kernbichler, A. F. Martitsch, and A. M. Runov, J. Phys.: Conf. Ser. **775**, 012001 (2016).

<sup>15</sup>R. Hager, C. S. Chang, N. M. Ferraro, and R. Nazikian, Nucl. Fusion **59**, 126009 (2019).

<sup>16</sup>A. I. Morozov and L. S. Solov'ev, Reviews of Plasma Physics **2**, 1 (1966).

<sup>17</sup>A. H. Boozer, The Physics of Fluids **23**, 904 (1980).

<sup>18</sup>R. G. Littlejohn, Journal of Plasma Physics **29**, 111 (1983).

<sup>19</sup>E. Hairer, C. Lubich, and G. Wanner, *Geometric Numerical Integration: Structure-Preserving Algorithms for Ordinary Differential Equations* (Springer Science & Business Media, 2006).

<sup>20</sup>P. J. Morrison, Phys. Plasmas **24**, 055502 (2017).

<sup>21</sup>R. Zhang, J. Liu, Y. Tang, H. Qin, J. Xiao, and B. Zhu, *Phys. Plasmas* **21**, 032504 (2014).

<sup>22</sup>B. Zhu, Z. Hu, Y. Tang, and R. Zhang, *Int. J. Model. Simulation, Sci. Comput.* **07**, 1650008 (2016).

<sup>23</sup>C. G. Albert, S. V. Kasilov, and W. Kernbichler, *Journal of Computational Physics* **403**, 109065 (2020).

<sup>24</sup>H. Qin and X. Guan, *Phys. Rev. Lett.* **100**, 035006 (2008).

<sup>25</sup>H. Qin, X. Guan, and W. M. Tang, *Phys. Plasmas* **16**, 042510 (2009).

<sup>26</sup>J. W. Burby and C. L. Ellison, *Phys. Plasmas* **24**, 110703 (2017).

<sup>27</sup>M. Kraus, arXiv preprint arXiv:1708.07356 (2017).

<sup>28</sup>C. L. Ellison, J. M. Finn, J. W. Burby, M. Kraus, H. Qin, and W. M. Tang, *Physics of Plasmas* **25**, 052502 (2018).

<sup>29</sup>M. Eder, C. G. Albert, L. M. P. Bauer, S. V. Kasilov, and W. Kernbichler, 46th EPS Conference on Plasma Physics **ECA Vol. 43C**, P5.1100 (2019).

<sup>30</sup>S. V. Kasilov, A. M. Runov, and W. Kernbichler, *Computer Physics Communications* **207**, 282 (2016).

<sup>31</sup>M. Drevlak, C. D. Beidler, J. Geiger, P. Helander, and Y. Turkin, 41st EPS Conference on Plasma Physics **ECA Vol. 38F**, P1.070 (2014).

<sup>32</sup>C. Grebogi and R. G. Littlejohn, *The Physics of Fluids* **27**, 1996 (1984).

<sup>33</sup>M. F. Heyn, I. B. Ivanov, S. V. Kasilov, W. Kernbichler, P. Leitner, V. V. Nemov, and W. S. and, *Nucl. Fusion* **54**, 064005 (2014).

<sup>34</sup>W. D. D'haeseleer, W. N. G. Hitchon, J. D. Callen, and J. L. Shohet, *Flux Coordinates and Magnetic Field Structure: A Guide to a Fundamental Tool of Plasma Theory* (2012).

<sup>35</sup>J. L. Velasco, K. Allmaier, A. Lopez-Fraguas, C. Beidler, H. Maassberg, W. Kernbichler, F. Castejon, and J. A. Jimenez, *Plasma Phys. Contr. Fus.* **53**, 115014 (2011).

<sup>36</sup>S. Matsuoka, S. Satake, R. Kanno, and H. Sugama, *Phys. Plasmas* **22**, 072511 (2015).

<sup>37</sup>B. Huang, S. Satake, R. Kanno, H. Sugama, and S. Matsuoka, *Phys. Plasmas* **24**, 022503 (2017).

<sup>38</sup>C. D. Beidler, K. Allmaier, M. Y. Isaev, S. V. Kasilov, W. Kernbichler, G. O. Leitold, H. Maassberg, D. R. Mikkelsen, S. Murakami, M. Schmidt, D. A. Spong, V. Tribaldos, and A. Wakasa, *Nucl. Fusion* **51**, 076001 (2011).

<sup>39</sup>H. Nyquist, *Transactions of the American Institute of Electrical Engineers* **47**, 617 (1928), conference Name: *Transactions of the American Institute of Electrical Engineers*.

<sup>40</sup>C. E. Shannon, Bell System Technical Journal **27**, 379 (1948).

<sup>41</sup>D. Reiter, M. Baelmans, and P. Börner, Fusion Science and Technology **47**, 172 (2005).